JATIS Journal of Astronomical Telescopes, Instruments, and Systems

RESEARCH PAPER

Transmission grating arrays for the X-ray spectrometer on Arcus Probe

Ralf K. Heilmann[a,*] Alexander R. Bruccoleri,[b] James A. Gregory[c] Eric M. Gullikson[d] Hans Moritz Günther[e] Edward Hertz[f] Renee D. Lambert,[c] Douglas J. Young,[c] and Mark L. Schattenburg[a]

[a]Massachusetts Institute of Technology, MIT Kavli Institute for Astrophysics and Space Research, Space Nanotechnology Laboratory, Cambridge, Massachusetts, United States
[b]Izentis, LLC, Cambridge, Massachusetts, United States
[c]MIT Lincoln Laboratory, Lexington, Massachusetts, United States
[d]Lawrence Berkeley National Laboratory, Berkeley, California, United States
[e]Massachusetts Institute of Technology, MIT Kavli Institute for Astrophysics and Space Research, Cambridge, Massachusetts, United States
[f]Harvard-Smithsonian Astrophysical Observatory, Center for Astrophysics, Cambridge, Massachusetts, United States

ABSTRACT. The Arcus Probe mission concept has been submitted as an Astrophysics Probe Explorer candidate. It features two co-aligned high-resolution grating spectrometers: one for the soft X-ray band and one for the far ultraviolet. Together, these instruments can provide unprecedented performance to address important key questions about the structure and dynamics of our universe across a large range of length scales. The X-ray spectrometer consists of four parallel optical channels, each featuring an X-ray telescope with a fixed array of 216 lightweight, high-efficiency, blazed transmission gratings, and two charge-coupled device readout arrays. Average spectral resolving power $\lambda/\Delta\lambda > 2500$ (3500 expected) across the 12 to 50 Å band and combined effective area > 350 cm^2 (>470 cm^2 expected) near OVII wavelengths are predicted, based on the measured X-ray performance of the spectrometer prototypes and detailed ray trace modeling. We describe the optical and structural design of the grating arrays, from the macroscopic grating petals to the nanoscale gratings bars, grating fabrication, alignment, and X-ray testing. Recent X-ray diffraction efficiency results from chemically thinned grating bars are presented and show performance above mission assumptions.

Keywords: Arcus; X-ray spectrometer; critical-angle transmission grating; high-resolution X-ray spectroscopy

Paper 24057SS received May 5, 2024; revised Aug. 30, 2024; accepted Sep. 5, 2024; published Sep. 30, 2024.

1 Introduction

Mere images or low-resolution spectra from celestial objects do not provide the required precision data that informs us about the kinetics and temperatures of baryons that underpin not only much of the visible universe but also trace the small and large-scale structure and dynamics of its hottest components as highly ionized plasma. Emission and absorption in these plasmas occur predominantly in the soft X-ray and far ultraviolet (FUV) bands, calling for high-resolution spectroscopy at these short wavelengths.[1] This is to quote the Astro2020 Decadal Review:[2]

*Address all correspondence to Ralf K. Heilmann, ralf@space.mit.edu

"Astronomy became astrophysics with the first spectrum. Spectroscopy determines compositions, magnetic field strength, space motion, rotation, multiplicity, planetary companions, surface structure, and other important physical traits..."

Arcus Probe (subsequently simply called Arcus) will carry the required state-of-the-art instruments that can deliver the desired spectra in much higher resolution and much shorter time than existing, aging X-ray observatories (as discussed in Sec. 6.3). The three baseline science goals of Arcus are "(i) exploring how supermassive black hole accretion and winds vary with luminosity, black hole mass, black hole spin and other parameters; (ii) determining how gas, metals, and dust flow into, through, and out of galaxies; and (iii) probing stellar activity across all stellar types and lifecycles, including exoplanet hosts targeted by current and future NASA habitable planet missions."[1]

Arcus features an X-ray spectrometer (XRS) ($\lambda = 1$ to 6 nm, $R = \lambda/\Delta\lambda = 3500$) and a co-aligned ultraviolet spectrometer (UVS) ($\lambda = 97$ to 158 nm, $R = 24{,}200$).[3] This combination will, for example, provide previously unachievable simultaneous high-resolution spectra of high-temperature X-ray lines (e.g., O VII, O VIII), warm adjacent ultraviolet (UV) ions (e.g., C II, Si III, O VI), and the cooler gas columns (e.g., H I), covering all phases of the cosmic web.

The main science cases for Arcus are discussed in more detail in Ref. 1, whereas Ref. 3 focuses more on time-domain science and opportunities for a general observer program for Arcus.

In the following, we first describe the structural and optical elements of the X-ray instrument, going from the largest to the smallest size scales. We then present how performance parameters are influenced by the macroscopic opto-mechanical instrument design, before discussing the nm- to mm-scale features of the individual grating elements. Grating fabrication is summarized briefly before we describe the X-ray performance of gratings and prototype spectrometers. We then compare performance and figures of merit with previous transmission grating (TG) technologies, model Arcus performance, and compare it with current X-ray spectroscopy missions. The alignment of the Si gratings to metal frames is described next, followed by the demonstration of a new method to reduce the width of the grating bars, leading to increased diffraction efficiency (DE) beyond Arcus requirements. We end by discussing future work and summarizing.

2 Arcus Probe X-ray Spectrometer

The XRS instrument consists of four parallel, almost identical optical channels (OC). In each channel, an array of grazing-incidence silicon pore optics (SPO),[4] with the layout of a sub-apertured version of the NewAthena design,[5] forms an X-ray telescope with a 12-m focal length. Sub-aperturing in azimuth for grazing-incidence mirrors leads to an anisotropic telescope point-spread function (PSF) that is much narrower in one dimension than for a mirror array that is fully populated in azimuth.[6,7] Just downstream of the X-ray mirrors follows a grating petal, carrying an array of 216 critical-angle transmission (CAT) gratings that cover the mirror array. CAT gratings are blazed transmission gratings that disperse soft X-rays into several diffraction orders, with the strongest orders on just one side of the image near twice the blaze angle of the gratings. The gratings are aligned with their dispersion axes parallel to the narrow direction of the PSF, minimizing the spectrometer line-spread function (LSF) in the dispersion direction. For the grating baseline design described in Sec. 4, some of the soft and most of the harder ($E \gtrsim 1.25$ keV) X-ray photons are not diffracted and form an image at the telescope focus, where X-ray charge-coupled devices (CCDs) provide energy resolution.[8] Effective area for harder X-rays in 0th order peaks around 1400 cm^2 near 1.8 keV and is still above 300 cm^2 at 6.7 keV (summed over all four OCs).[9]

The combination of optics and grating petals comprises an OC. The four OCs are mounted to a common forward assembly, which in turn is mounted to a coilable boom that is stowed during launch and deploys/uncoils after orbit insertion (see Fig. 1). The boom is connected on the other end to the rear assembly, which serves as the interface to the spacecraft and holds the two CCD detector subsystem assemblies (DSA), plus other systems. Information about an earlier version of the boom can be found in Ref. 10.

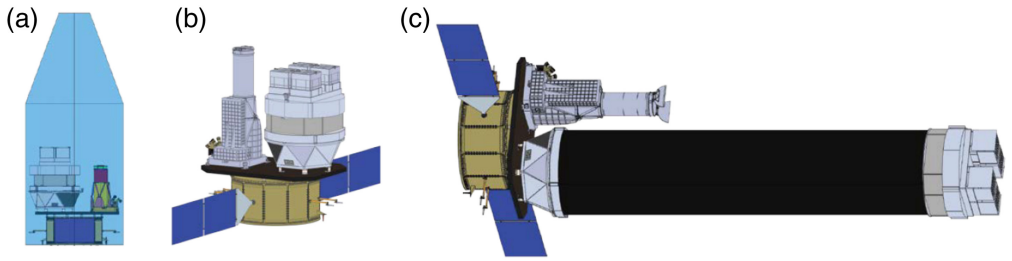

Fig. 1 Arcus Probe schematics. (a) Spacecraft with instruments stowed in launch vehicle fairing. (b) In space after solar panel deployment deployment. The UVS is on the left and the XRS on the right. (c) After XRS boom deployment.

The gratings in each channel are placed along the surface of a tilted Rowland torus that also contains the telescope focus. This guarantees that the best focus in the dispersion direction for the non-zero orders is achieved and also lies on the Rowland torus surface. One DSA (DSA-1) sits at the focus of optical channels OC-1 and OC-2. DSA-2 collects the strong blazed orders from OC-1 and OC-2. Due to the symmetries of the design, DSA-2 can simultaneously lie on the differently tilted Rowland torus for OC-3 and OC-4 and their foci. The gratings in the latter two channels are blazed in the opposite direction from the gratings in the first two channels, creating strong, focused diffraction orders on DSA-1 (see Fig. 2). Each OC is offset from the others by a few mm in the cross-dispersion direction, leading to four quasi-(anti)-parallel spectra collected by only two compact DSAs. This so-called double-tilted Rowland torus design combines dense stacking of sub-apertured, narrow-LSF optics in a limited aperture, with a minimal number of readout CCDs. It is described in detail in Refs. 11 and 12. The readout cameras are described in detail in a separate paper of this Special Section.[8]

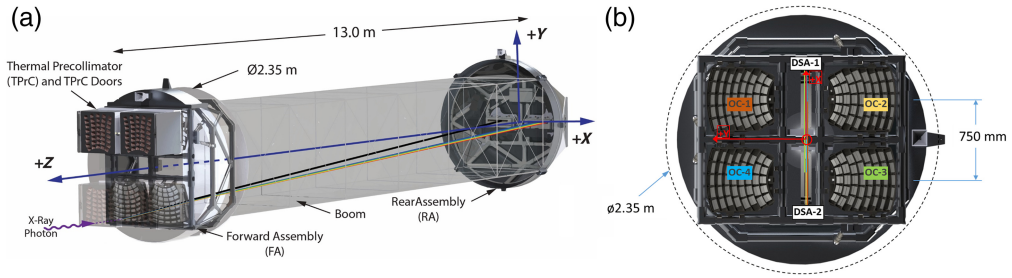

Fig. 2 Layout of the XRS. (a) Angled view, showing the thermal precollimators and SPO arrays for the four OCs on the left. The grating petals are obscured behind the SPO arrays. An X-ray is shown that enters the lower left OC (OC-3) and either lands at the telescope focus (black line to DSA-2) or gets diffracted into a blazed order (rainbow colors to DSA-1). (b) View from the X-ray source into the XRS, showing the four OCs and the two DSAs.

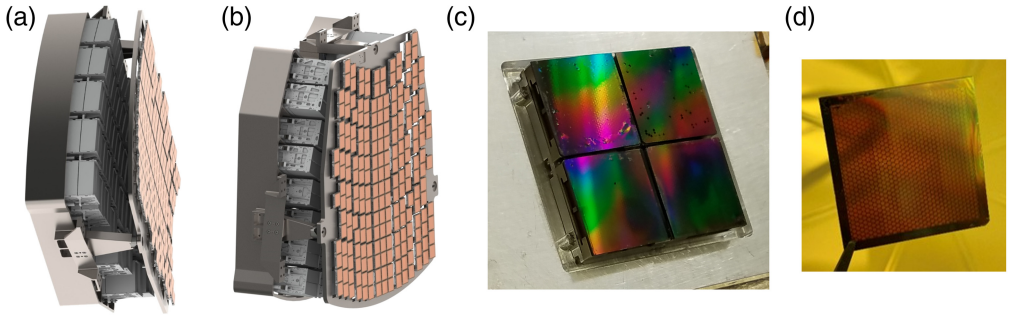

Fig. 3 (a) and (b) Two different views of an optical channel. The grating petal, holding 40 grating windows with a total of 216 grating facets, follows the shape of the Rowland torus. (c) Prototype grating window with four 32.5×32 mm^2 CAT grating facets. (d) Silicon grating membrane, held by tweezers.

A grating facet consists of a 32.5×32 mm^2 silicon membrane aligned and bonded to a metal facet frame.[13] All grating facets for all channels have the same design, are operationally identical, and can be exchanged with each other. Blazing is simply achieved through proper tilting relative to the incident X-rays. The grating facets are mounted to grating windows in groups of 4 to 6. The windows are designed to cover the SPO beams with the minimum number of gratings of the given size (see Fig. 3).

3 Predicted XRS Performance

The key performance parameters for the XRS are effective area (A_{eff}) and resolving power ($R = \lambda/\Delta\lambda$), with λ being the X-ray wavelength and $\Delta\lambda$ the smallest wavelength difference that can be resolved. Effective area is mainly determined by the mirror effective area that feeds the grating array, grating DE summed over the collected diffraction orders, geometrical loss factors (X-ray blockage from support structures, gaps between gratings and CCDs), filter transmission, and CCD quantum efficiency. Resolving power to first order is given by the diffraction angle of a given diffraction order, divided by the spectrometer LSF. CAT gratings are blazed transmission gratings that have advantages in DE and resolving power for $\lambda \gtrsim 1$ nm compared with existing grating instruments on Chandra[14] and XMM/Newton.[15] To estimate XRS performance, we need to understand the blazing principle underlying CAT grating design and the alignment tolerances that affect both A_{eff} and R. Alignment tolerances are derived from detailed ray tracing that is described elsewhere in this Special Section and for previous smaller versions of Arcus.[9,16]

4 CAT Grating Principle and Structural Hierarchy

CAT gratings feature ultra-high aspect ratio and freestanding grating bars with nm-smooth sidewalls.[17] Each grating is inclined such that X-rays of wavelength λ impinge on the grating bar sidewalls at graze angles α below the critical angle for total external reflection α_c (see Fig. 4). The critical angle depends on λ and the grating bar material. The bandpass of the gratings is limited toward short λ by the chosen combination of α and bar material.

The diffraction angle β_m for the mth diffraction order is given by the grating equation

$$\frac{m\lambda}{p} = \sin\alpha - \sin\beta_m, \tag{1}$$

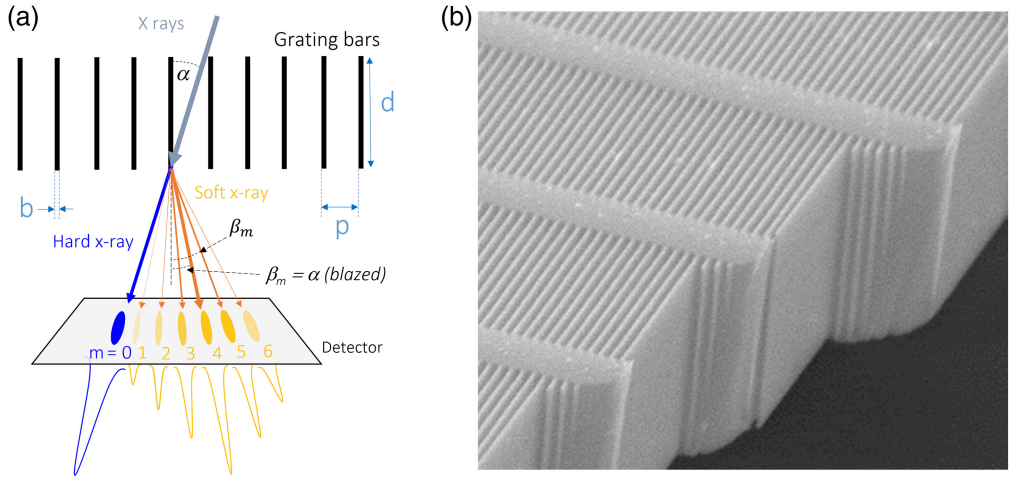

Fig. 4 (a) Schematic cross-section through a CAT grating of period p. The mth diffraction order occurs at an angle β_m where the path length difference between X-rays from neighboring grating slots is $m\lambda$. The straight-through beam ($m = 0$) is shown in blue. Orders near where β_m coincides with the direction of specular reflection from the grating bar sidewalls ($|\beta_m| = \alpha$) are enhanced, i.e., these orders are blazed. (b) Scanning electron micrograph (SEM) of a cleaved CAT grating membrane showing top, cross-section, and sidewall views of the 200 nm-period silicon grating bars and their monolithically integrated 5-μm period L1 cross supports (X-rays enter from the top and leave out the bottom).

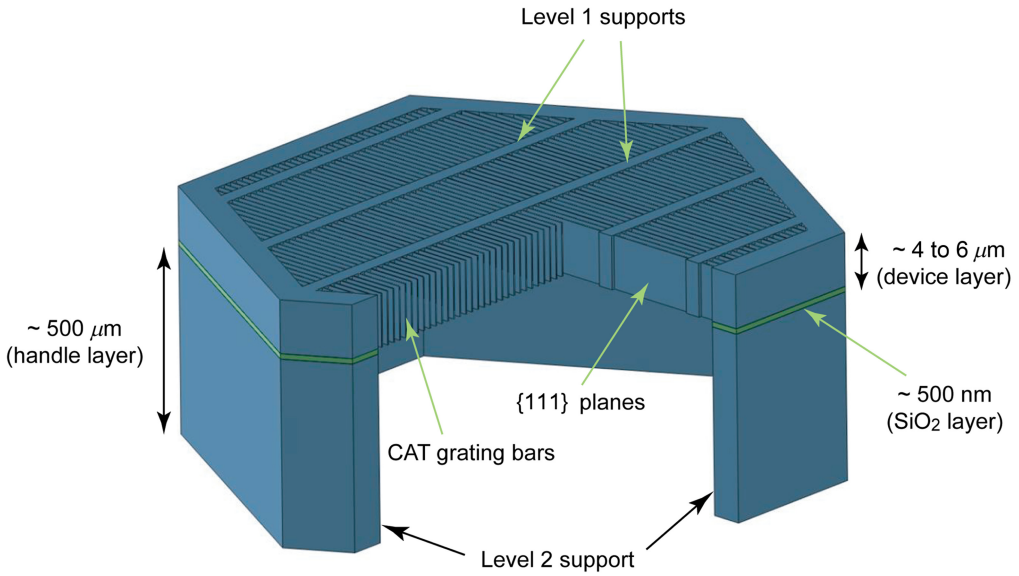

Fig. 5 Schematic showing the structural hierarchy of a CAT grating membrane (not to scale). See text for details.

where p is the grating period. In analogy with sawtooth reflection gratings, diffraction orders near the direction of specular reflection from the sidewalls show increased efficiency (i.e., blazing, with α being the blaze angle). In a simplified geometrical optics picture, blazing is most efficient when $\tan\alpha \approx (p-b)/d$, where b is the grating bar width and d is the grating bar depth (see Fig. 4). In addition, each pair of neighboring grating bars forms a slit that causes diffraction. The blazed orders extend over the "blaze envelope," which is centered on the specular reflection direction and whose width is proportional to $\lambda/(p-b)$.[18] The small critical angles for soft X-rays reflecting off Si on the order of 1 deg to 2 deg demand high-aspect ratio grating bars to intercept all incoming photons. Furthermore, the bars should be as thin as possible to minimize blockage and absorption. For a fixed grating period, the ability to fabricate higher aspect ratio grating bars is necessary to extend the bandpass with high efficiency to shorter λ. The grating period cannot be too large compared to the X-ray wavelength to obtain diffraction orders that can be sorted by order using the energy resolution of Si-based detectors. The baseline design initially chosen and fabricated for Arcus has $p = 200$ nm, $d = 4$ μm, and $b \approx 70$ nm, corresponding to $\alpha \approx 1.9$ deg. Recently, we also demonstrated $d > 5.5$ μm.[19]

CAT grating bars are not supported by a membrane but are freestanding. As seen in Fig. 4(b), the bars are held in place by a monolithically integrated 5-μm period level 1 (L1) support mesh. Additional support structures are needed for the few-μm thin grating layer to manufacture large enough CAT gratings that can cover large areas on the order of thousands of square centimeters with a manageable number of gratings. Figure 5 shows the additional, much thicker, and stronger level 2 (L2) hexagonal support structure on the scale of ~1 mm.

5 CAT Grating Fabrication

CAT grating fabrication has been described extensively in previous work and is briefly summarized here.[20,21] CAT gratings are currently made from 200 mm silicon-on-insulator (SOI) wafers. The thin Si device ("front side") layer of the SOI wafer is manufactured to thickness d (see Fig. 4).

Using 193 nm 4X optical projection lithography (OPL) at MIT Lincoln Laboratory, patterns for CAT gratings, L1, and L2 structures are simultaneously transferred into a silicon oxide layer that serves as a mask for the subsequent deep reactive-ion etch (DRIE). The ~0.6-mm-thick handle ("backside") layer of the SOI wafer is then DRIE'd with a hexagonal pattern that has been aligned with the front side L2 hexagons using a maskless aligner. The grating bars are aligned parallel to the vertical {111} planes of the (110) device layer. Since DRIE leaves rough sidewalls, this crystal orientation is used to "polish" the grating bar sidewalls post-DRIE through

immersion in a potassium hydroxide solution.[17] The gratings have to be dried in a critical-point dryer to prevent stiction due to liquid-vapor surface tension. Finally, the buried oxide layer separating the device and handle layers is removed in the areas not covered by Si, resulting in a monolithic Si grating layer with freestanding CAT grating bars, integrated L1 and L2 supports, and a bulky L2 mesh.

CAT gratings can be fabricated in volume manufacturing mode from 200 mm SOI wafers,[21] in principle allowing for ~16 to 20 gratings to be produced from a single wafer.

6 CAT Grating X-ray Performance

The main performance requirements for X-ray diffraction gratings are high DE and enabling high resolving power in a spectrometer instrument.

6.1 Diffraction Efficiency

DE has been measured repeatedly at beamline 6.3.2 of the Advanced Light Source at Lawrence Berkeley National Laboratory. The focused, tunable monochromatic X-ray beam has a small enough diameter to be placed within a single L2 hexagon, but it integrates over many tens of L1 periods. A slit-covered photodiode detector is placed at the angle of a transmitted diffraction order, and the grating is rotated to measure DE over a range of several degrees in incidence angle. The detector remains in place during grating rotation since the change in diffraction angle as a function of grating rotation is negligible. This is a major advantage of the transmission geometry since this also means that certain grating alignment tolerances are very relaxed compared to reflection gratings.

DE can be modeled using rigorous coupled-wave analysis (RCWA).[22] Typically, CAT gratings perform in the range of 80% to 100% of RCWA predictions for DE, where the difference from 100% can often be modeled heuristically with a Debye-Waller-type (DW) roughness factor $f_{\mathrm{DW}} = \exp[-(2\pi m\sigma/p)^2]$, where σ could be interpreted as a sidewall roughness.[21] Current prototypes with 200 nm period, $d = 4$ μm, and $b \approx 60$ to 70 nm deliver DE $> 20\%$ in individual orders and $> 30\%$ when summed over the strongest ("blazed") orders ($\beta_m \sim |\alpha|$) near O-K wavelengths (see Fig. 6). These numbers include losses caused by absorption from the L1 supports.

Several 4 μm-deep gratings were measured at several wavelengths, and the data is modeled with RCWA and a DW factor (see Fig. 6(b) for an example). The model is then used to extrapolate efficiency between the measured wavelengths and angles as an input for ray-trace-based effective area predictions for the XRS. Ray tracing also takes into account alignment tolerances and the changing efficiencies as a function of grating angles.[9,24]

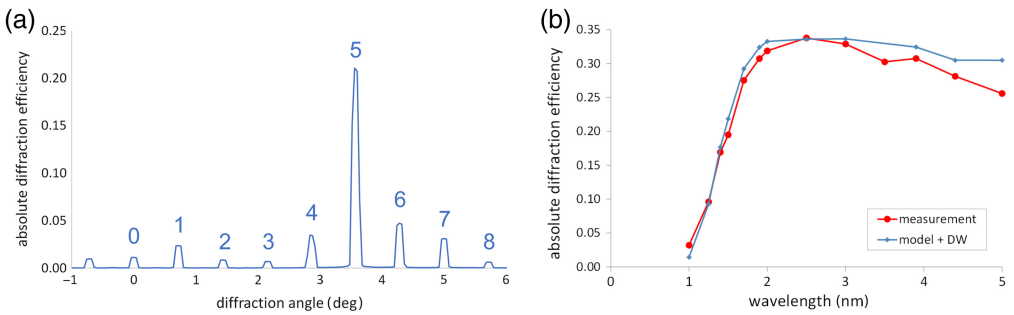

Fig. 6 Representative DEs of 4-μm deep CAT gratings from synchrotron data. (a) Example detector scan as a function of angle relative to 0th order for $\lambda = 2.5$ nm and sidewall incidence angle of 1.75 deg. DE is strongly blazed for the 5th order at 21%. Summing over orders 4 to 7 gives a total DE of 32.2%. These values include absorption by L1 bars, but not blockage by the L2 mesh. (b) Comparison of model efficiency (sum of blazed orders collected by XRS readouts), multiplied by Debye-Waller-like roughness factor, for 82% L1 open area fraction with synchrotron spot measurements (sum of the same blazed orders as for model) for a 32.5×32 mm^2 CAT grating.[23] The L2 mesh is not considered in this plot.

The synchrotron beam can be scanned over a whole grating to examine uniformity of efficiency.[13,23,25] Alternatively, we also measured efficiency in the converging beam of an SPO, almost fully illuminating a large CAT grating in an Arcus-like configuration, and verified that it agreed with synchrotron spot measurements and exceeded model assumptions.[26]

6.2 Resolving Power

Resolving power R is an expression of how much a spectral line is broadened by the XRS response function. The main ingredients are the mirror LSF (PSF projected onto the dispersion axis), the diffraction angles of the measured orders, the distance of the gratings from focus, the aberrations of the optical design, the CCD pixel size, and grating imperfections. Large R requires a large grating distance from focus and large diffraction angles, and small values for the other terms.

The most obvious grating imperfection that would limit R is a variation Δp of grating period p, since it would introduce a variation in β_m [see Eq. (1)]. For a Gaussian distribution of Δp one can define an effective grating resolving power $R_g = p/\Delta p$ as an additional term in the instrument response function that contributes to the broadening of measured spectral lines.[26] R_g is an upper limit to the resolving power of the XRS and can be measured in the following way: First, the PSF of a focusing optic (the "direct beam") is measured with a narrow-line soft X-ray source, such as the well-characterized Al-K$_\alpha$ doublet. Then, a grating is inserted into the beam, and the source spectrum is measured in the highest accessible diffraction order. The measured spectrum is a convolution of the known source spectrum with the measured LSF of the direct beam and a Gaussian of width $\Delta\beta_m$ caused by Δp. Thus, Δp and R_g can be extracted from fitting to the measured spectrum. (Other potential contributions to spectral broadening are ignored, making this a conservative measurement of R_g.) This measurement has been performed on many different 200-nm period CAT gratings up to 18th order ($|\beta_{18} - \beta_0| = 4.3$ deg) at the Marshall Space Flight Center Stray Light Facility using a slumped glass mirror pair[23,25,27] and up to 21st order at the PANTER X-ray facility using an SPO.[21,26] In all cases, $R_g \approx 10^4$ was found, which significantly exceeds the $R_g > 3850$ Arcus requirement.

A linear array of four co-aligned CAT gratings, illuminated by a pair of confocal SPOs in an Arcus-like setup, also performed as expected.[13] As shown in Fig. 7, we recently derived $R_g \approx 1.3^{+\infty}_{-0.5} \times 10^4$ (3σ) for a different pair of co-aligned gratings, simultaneously illuminated by a single SPO with LSF ~1 arcsec [full-width half max (FWHM)].[26]

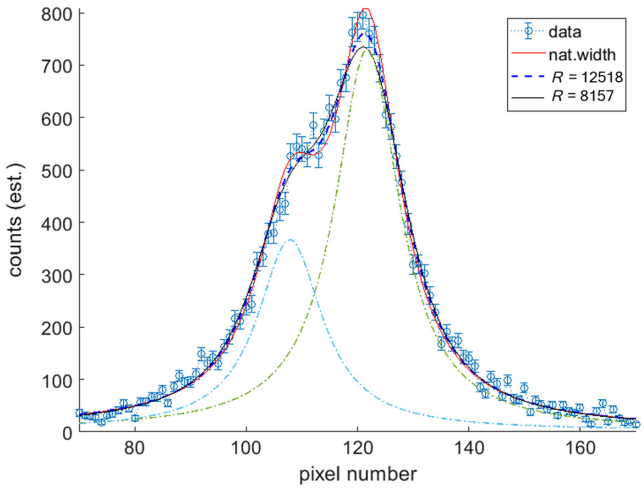

Fig. 7 Spectrum of Al anode from two mutually aligned and simultaneously illuminated CAT gratings, showing the Al-K$_\alpha$ doublet measured in 18th order.[26] Camera pixels are 20 μm in size. The red line is the natural line shape of the doublet,[27] and the dashed line is the best fit to the data. The black solid line is the curve for the lower 3σ confidence limit, corresponding to $R_G = 8157$. The upper 3σ confidence limit includes $R = \infty$. The dash-dotted lines show the individual $K_{\alpha 1}$ and $K_{\alpha 2}$ components with their natural widths on top of the weak sloped background.

In total, over a dozen different individual CAT gratings with d between ~3 and ~6 μm, metal-coated[25,27] and uncoated, and patterned using interference lithography or OPL, have been measured, and $R_g \sim 10^4$ has always been found, attesting to the narrow grating period distribution.

The limiting factor in resolving power for the Arcus XRS therefore is not the quality of CAT gratings, but the combined LSF from the whole OC SPO petal, required to be <3.4 arcsec (FWHM), and expected to be 2.6 arcsec (FWHM).

6.3 XRS Figures of Merit

It is useful to discuss the leap in performance that CAT grating technology provides in the soft X-ray band over previous X-ray grating technologies.

The high- and low-energy transmission grating spectrometers (HETGS,[14] $p = 200$ (HEG) and 400 nm (MEG); and LETGS,[28] $p = 991$ nm) on Chandra have the advantage of small mirror LSF on the order of 0.5 arcsec, but most of the diffracted photons land at small angles in $m = \pm 1$st orders ($\beta_m \approx \lambda/p = 1 - 25 \times 10^{-3}$ rad for the 1 to 5 nm wavelength band). For the Arcus XRS, CAT gratings are inclined by 1.8 deg relative to the incident X-rays, and the strongest orders are found near $\beta_m = 0.063$ rad, relatively independent of λ. Chandra gratings were designed as phase-shifting gratings with high efficiencies below 1 nm and peaking near 0.7 nm wavelength. Figure 8(a) compares DEs for different grating types. CAT gratings are designed for broadband high efficiency for wavelengths longer than 1 nm. Arcus assumes performance shown as "4 μm CAT." The "6 μm CAT" curve shows results from deeper, more recent gratings with $d \sim 5.5$ to 6 μm that could be used instead, which could improve Arcus effective area further, especially if used at slightly smaller α. Figure 8(b) is a direct comparison, assuming CAT gratings were placed on Chandra. It shows a figure of merit for the detection of absorption lines, which is proportional to $\sqrt{A_{\rm eff} \times R}$. We conservatively limited R to 10^4, even though the Chandra mirror LSF would allow for higher values of R. CAT gratings outperform Chandra gratings significantly for $\lambda > 1$ nm.

Figure 9 compares two different figures of merit for actual instruments on different missions with the predicted Arcus performance. Despite the wider LSF compared with Chandra, the Arcus XRS is expected to exceed Chandra HETG and XMM/Newton RGS figures of merit by 1 to 2 orders of magnitude across the 1 to 5 nm band, due to a combination of CAT grating properties and the larger mirror effective area. Also shown is the Resolve instrument on XRISM, which is a

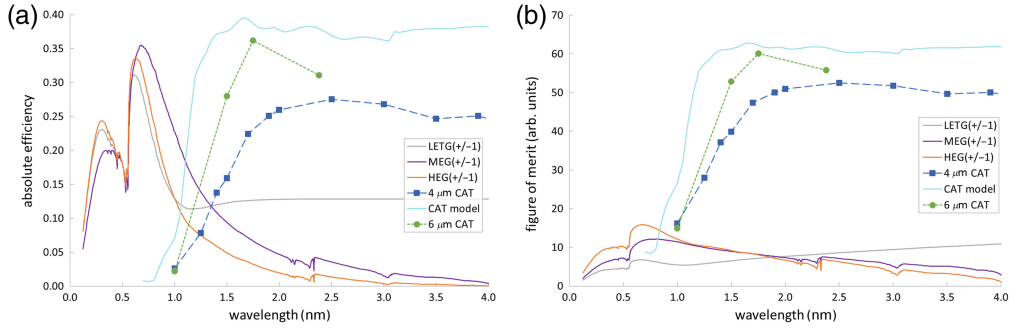

Fig. 8 Comparison of TG diffraction efficiencies and figure of merit. (a) For Chandra gratings, the sum of ±1st order DEs from calibration files is shown.[29] These DEs include all losses from support structures and gaps between facets. For CAT gratings, all orders within the blaze envelope are summed up, and a total loss of 31% from support structures and gaps is assumed. "4 μm CAT" is from synchrotron measurements of a CAT grating with $d \approx 4\mu$m, $b \approx 80$ nm, and $\alpha = 1.85$ deg, while "6 μm CAT" is from a grating with $d \approx 6$ μm and $b \approx 60$ nm, measured at $\alpha = 1.5$ deg. The latter are from the first prototypes of this thickness.[19,30] "CAT model" is the sum of blazed order DEs from a model with $d = 6$ μm, $b = 40$ nm, $\alpha = 1.5$ deg, and $\sigma = 1.5$ nm DW roughness parameter. (b) Figure of merit for weak line detection ($\sim\sqrt{A_{\rm eff}R}$). The same mirror effective area and constant detector efficiency are assumed for all plots. For CAT gratings, $R = 10^4$ is assumed as an upper limit, based on conservative analysis of lab measurements.[25–27] The HETG and LETG instruments complement each other over the shown range. Chandra with CAT gratings would be superior by far for $\lambda > 1$ nm due to a combination of higher DE and blazing into higher orders.

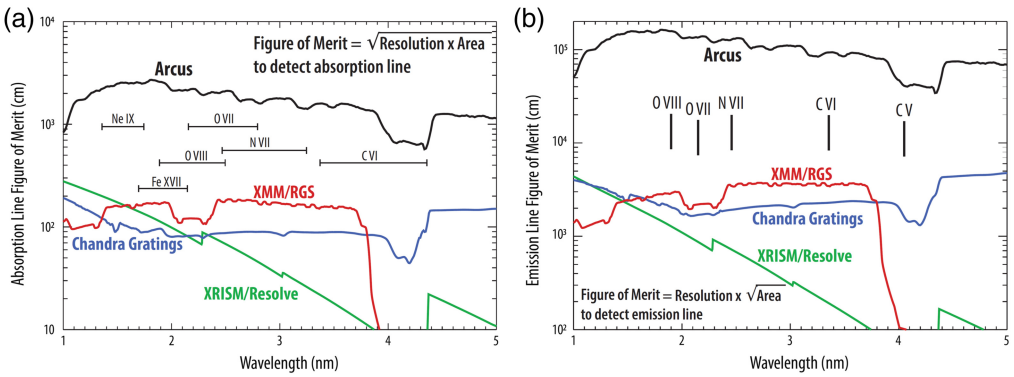

Fig. 9 Comparison of figures of merit between soft X-ray spectroscopy instruments in operation and the Arcus Probe XRS. "Chandra Gratings" refers to the better of HEG, MEG, and LETG. The curve for the resolve microcalorimeter on XRISM[31] assumes that the closed aperture door is open. The wavelength ranges for important plasma diagnostics lines are also indicated. (a) Figure of merit for absorption line detection. (b) Figure of merit for emission line detection.

microcalorimeter with a fixed energy resolution of slightly below 5 eV. It provides better performance at much shorter wavelengths than shown.[31]

7 CAT Grating Alignment

Alignment tolerances for CAT gratings are derived using ray-tracing models as described in Refs. 9, 11, and 16.

Positioning tolerances are in the 200 μm to mm (3σ) range, well within precision machining capabilities. Two rotational degrees of freedom require custom metrology for alignment before the grating membrane is bonded to its metal facet frame:

The grating roll (rotation around the grating normal, which also rotates the dispersion axis) can be measured using visible light diffraction from the L1 cross support mesh,[19] which is defined in the OPL mask to be oriented at 90 deg from the CAT bars.[21] Before bonding, the roll relative to the facet frame sides is adjusted to be the same for all grating facets, using a reference grating facet.

Grating yaw, which controls the angle of incidence onto the CAT grating bar sidewalls, requires a separate measurement of the grating bar tilt relative to the grating membrane surface normal using small-angle X-ray scattering.[32] Using laser reflection, the measured bar tilt is then compensated for during the bonding of the Si membrane to its metal frame, such that the average grating bar direction ends up being parallel to the normal of the facet frame bottom, which is the mechanical reference surface for mounting to the grating window. The success of this alignment method within Arcus tolerances was demonstrated with X-rays for a 2×2 grating window.[26]

8 Increasing Diffraction Efficiency Through Bar Thinning

Besides fabricating CAT gratings with $d > 4$ μm and reducing the cross sections of support structures, XRS effective area can also be improved by reducing the grating bar width b. The fabrication method described above typically results in bar widths in the 60-nm range. Smaller widths could in principle be achieved by creating an oxide mask with a lower duty cycle (the ratio of mask line width to grating period). However, the resulting thinner bars can suffer from increased damage and destruction during the more aggressive wet etching and cleaning steps. Obviously, thicker bars are less fragile and preferred during wet processing steps.

Grating bar width can be reduced after the above fabrication steps using repeated cycles of oxidation—which consumes a small amount of Si—and oxide removal using hydrofluoric acid (HF) vapor. Both steps are gas-based and gentle. In the first set of experiments, we demonstrated bar thinning on gratings that were not freestanding, simply by removing native oxide with HF vapor, letting the native oxide layer reform in air, and repeating the cycle.[33] (We believe the etch rate derived in Ref. 33 has been overestimated and plan to reanalyze the data.) We subsequently repeated the experiment on three freestanding gratings, after measuring their DE. Thinning is

observable in top and bottom SEM images after about 10 cycles. Here, we present the first comparisons of DE before and after bar thinning.

Of the three tested gratings with $d \sim 6$ μm, one each underwent 10 (SP1), 20 (SP3), and 30 (SP5) cycles of HF vapor oxide removal and native oxide regrowth. The oxide was allowed to reform for at least 24 h before the next HF vapor etch. Figure 10 shows top-down SEM images of grating SP3 before and after treatment. After image analysis, we estimate the CAT grating bars to be 4 ± 2 nm thinner, changing from ~57 to ~53 nm at the top. Changes in thickness b deeper into the gratings obviously cannot be discerned from SEM images. For grating SP1, we cannot detect any clear changes. The changes for grating SP5 look similar to the ones for SP3.

The gratings were measured for DE at the synchrotron 11 months after their initial synchrotron measurements and about 2 months after the start of the HF vapor etching cycles. Measurements were taken with a sub-mm footprint beam in the center of the same L2 hexagon as before on each sample, except for SP1, which unfortunately was damaged during handling in the area of the previously measured hexagon. For SP1, another hexagon near the original location was selected, and we could not discern a systematic increase or decrease in DE. Based on experience, we do not expect changes in DE due to imperfect beam centering within a hexagon.

For gratings SP3 and SP5, we show DE comparisons in Fig. 11. One can clearly see an increase in 0th-order efficiency, especially at normal incidence, which indicates less blockage by Si. For individual higher diffraction orders, the DE increase is less pronounced, but it is clearly visible when summing over the blazed orders. For both gratings, we find an increase in blazed efficiency in the range of 2% to 3% in the angular range where blazing is most efficient. Preliminary modeling of the DE with RCWA, dividing the grating bars into multiple layers with

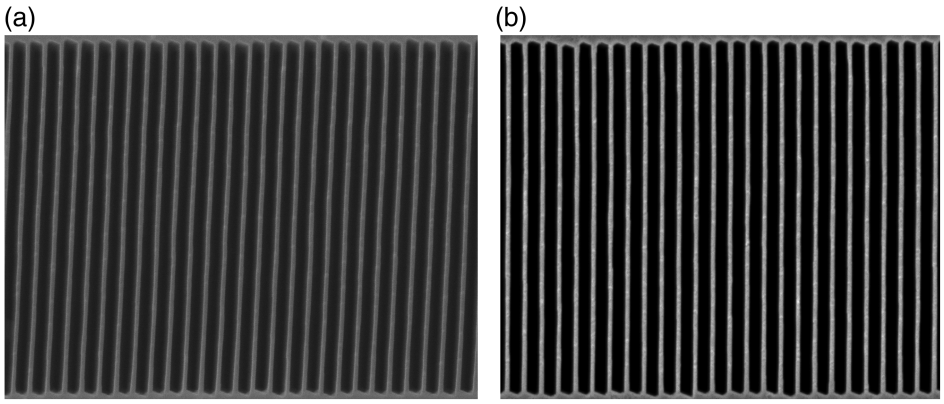

Fig. 10 Top-down SEM images of grating SP3 before (a) and after 20 cycles of HF vapor etching and oxidation in ambient air (b), showing that the treatment has not introduced visible damage to the grating bars. The 200 nm-period grating bars are slightly thinner after 20 cycles, but the difference is difficult to quantify precisely from SEM images alone.

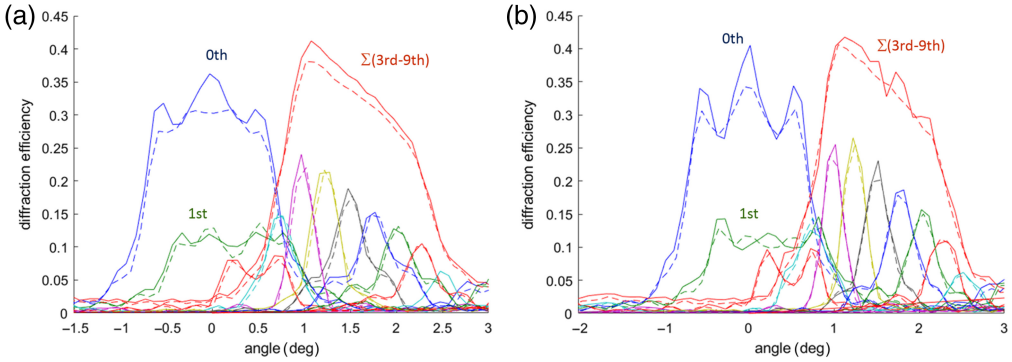

Fig. 11 Diffraction efficiencies at $\lambda = 1.75$ nm for orders 0 to 10 and sum of orders 3 to 9 as a function of incidence angle. Dashed lines are before thinning, and solid lines are after thinning. (a) Grating SP3. (b) Grating SP5. The repeatability of these measurements is better than 1%, i.e., a DE value of 0.4 has an uncertainty below 0.004.

independent parameters, indicates that the CAT grating bars became ∼4 to 5 nm thinner on average, with average b approaching ∼42 to 44 nm. The curves for 0th-order efficiency are very sensitive to the detailed grating bar profile and show meaningful differences between SP3 and SP5 before as well as after thinning. (In our heuristic approach of modeling roughness with a DW factor the 0th-order DE is insensitive to roughness.) The data also show that DE is significantly higher than assumed for Arcus (see Fig. 6).

In Fig. 12, we show model predictions for a CAT grating with rectangular grating bars and $\sigma = 2.5$ nm that has been thinned from 56 to 50 nm. It demonstrates how thinning changes DE, which is very similar to what we observe in our X-ray data: An increase in DE for the sum of orders around 2%, and high sensitivity of 0th-order DE to small changes in bar geometry. Included in Fig. 12 is the ideal case for the sum of orders without a roughness factor, showing how significant gains in efficiency can be made if grating bar profiles can be made as smooth as possible.

While our results show that HF vapor etching of silicon oxide leads to thinner grating bars, the etch could also change the roughness of the sidewalls, thereby increasing (lower roughness) or decreasing (higher roughness) DE. Our X-ray data do not indicate a significant change in roughness.

It is unclear why 10 treatment cycles seem to have caused little change and why we see little difference in outcome between 20 and 30 etch/oxidation cycles. We plan to perform more systematic experiments, including the fast growth of thicker oxide layers in a single step at elevated temperatures, to understand the different trade-offs between experimental conditions and outcomes.

There will be a mechanical limit to making grating bars thinner when the grating membrane could get damaged by launch vibrations. Vibration and temperature cycling testing so far have not revealed any problems,[23] but will have to be repeated for thinner structures.

Deeper gratings with thinner bars lead to higher DE, but a comparison of Figs. 6 and 11 shows, not necessarily near $\alpha \approx 1.8$ deg for the given examples. Arcus can be designed for smaller α, but maintaining the same resolving power might then require narrower LSF and/or tighter alignment tolerances. The detailed trade-offs are complex and beyond the scope of this work.

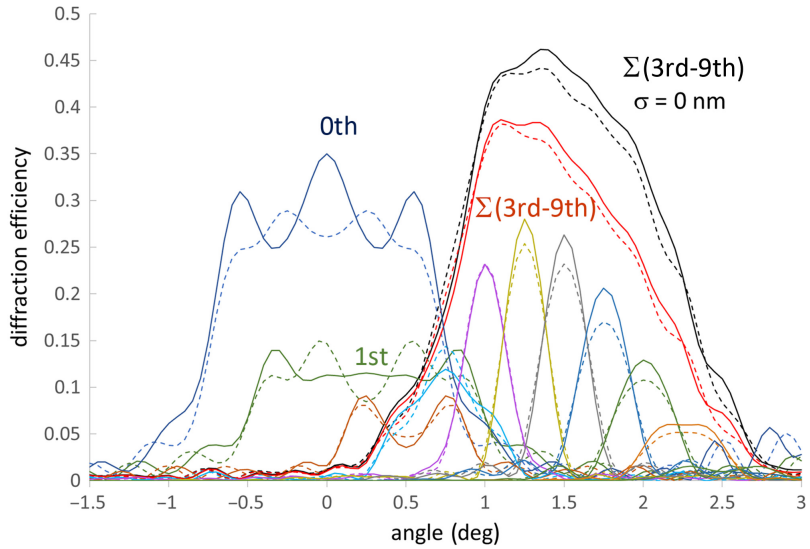

Fig. 12 RCWA model DEs for an Si CAT grating at $\lambda = 1.75$ nm for orders 0 to 10 and the sum of orders 3 to 9 (red) as a function of incidence angle. Dashed lines are before thinning, and solid lines are after thinning. The model assumes $p = 200$ nm, $d = 5.8$ μm, $b = 56$ nm (before thinning), and 50 nm (after thinning). A roughness factor using $\sigma = 2.5$ nm is applied. The sum of orders for $\sigma = 0$ nm is shown in black. An L1 open area fraction of 78% is assumed, which is the same as for gratings SP3 and SP5.

9 Future Work

Future improvements in DE are possible through thinner CAT grating bars and thinner L1 and L2 support structures. The Arcus Probe XRS assumes an L1 duty cycle of 18%, but large CAT gratings with a 10% duty cycle have been fabricated previously[34] and could be used for Arcus. The L2 open area fraction could be increased from the current 81% to a higher value. Deeper gratings also show higher DE, but the difference with 4-μm deep gratings is most pronounced at smaller incidence angles, which are preferred for larger mission concepts with smaller optics PSF, such as Lynx.[35,36] All of these improvements are actively being investigated. CAT gratings have been coated conformally with thin films of Pt, which increases the critical angle and/or extends the bandpass to shorter wavelengths.[25] Metal coating adds a useful variable to the grating design parameter space.

10 Summary

Arcus Probe is a mission concept that features two high-resolution spectrometers. The XRS described in this work is an instrument with 1 to 2 orders of magnitude improved performance compared to existing missions in the 1 to 5 nm soft X-ray band. The four parallel OCs with their shared readouts provide a large effective area and high redundancy in a small footprint. This work focuses on the CAT grating arrays, which—together with SPO petals—make up the OCs. We presented the array and grating optical and mechanical design, from the meter to the nanometer scale. Demonstrated X-ray performance of gratings and prototype spectrometers is discussed. Alignment tolerances are well-understood and well within metrology and manufacturing capabilities. Co-alignment with the UVS is described in another paper in this Special Section,[37] as well as the UVS itself.[38]

SPOs and CAT gratings already perform at required levels or exceed them. The effective area can be increased further through the reduction of blockage by grating bars and support structures. A volume manufacturing approach utilizing tools from the semiconductor and MEMS industries has been developed that can produce the required 864 CAT gratings efficiently in 2 years.[21] Mechanical structures (facet frames, grating windows, grating petals, etc.) are standard precision engineering items.

The XRS OC design is mature, and its components are well-understood, tested, and perform at required levels or better.

Disclosures

Several authors of this paper are members of the Arcus collaboration. Should NASA select Arcus for implementation, their institutions will receive funding that may be used to fund the authors' salaries in full or in part in the future.

Code and Data Availability

Data presented in this paper can be made available by the author (RKH) upon reasonable request.

Acknowledgments

This work has been funded in part under NASA (Grant Nos. 80NSSC22K1904 and 80NSSC250K0780) and by the MIT Kavli Institute for Astrophysics and Space Research. We appreciate facility support from MIT.nano. This research also used resources from the Advanced Light Source (beamline 6.3.2), a U.S. DOE Office of Science User Facility (Grant No. DE-AC02-05CH11231).

References

1. R. Smith, "The Arcus Probe mission," *Proc. SPIE* **12678**, 126780E (2023).
2. National Academies of Sciences, Engineering, and Medicine, *Pathways to Discovery in Astronomy and Astrophysics for the 2020s*, National Academies Press, Washington, DC (2021).
3. R. K. Smith et al., "The Arcus Probe mission," *Proc. SPIE* **13093**, 1309326 (2024).
4. B. Landgraf et al., "High-resolution and light-weight silicon pore x-ray optics," *Proc. SPIE* **12679**, 1267903 (2023).

5. M. Bavdaz et al., "NewATHENA optics technology," *Proc. SPIE*, **12679**, 1267902 (2023).
6. W. Cash, "X-ray optics. 2. A technique for high-resolution spectroscopy," *Appl. Opt.* **30**, 1749–1759 (1991).
7. R. K. Heilmann et al., "Critical-angle transmission grating spectrometer for high-resolution soft x-ray spectroscopy on the International X-ray Observatory," *Proc. SPIE* **7732**, 77321J (2010).
8. C. Grant, "Arcus focal plane cameras," *J. Astron. Telesc. Instrum. Syst.* **11**(1) (2025).
9. H. M. Günther and R. K. Heilmann, "Arcus x-ray telescope performance predictions and alignment requirements," *J. Astron. Telesc. Instrum. Syst.* **11**(1) (2025).
10. H. Bergner et al., "Development of a 12m coilable boom for the Arcus MIDEX mission," *Proc. SPIE* **11821**, 118211E (2021).
11. H. M. Günther et al., "Performance of a double tilted-Rowland-spectrometer on Arcus," *Proc. SPIE* **10397**, 103970P (2017).
12. H. M. Günther et al., "Concept of a double tilted Rowland spectrograph for X-rays," *ApJ* (2024).
13. R. K. Heilmann et al., "Blazed transmission grating technology development for the Arcus x-ray spectrometer explorer," *Proc. SPIE* **10699**, 106996D (2018).
14. C. Canizares et al., "The Chandra high-energy transmission grating: design, fabrication, ground calibration, and 5 years in flight," *Publ. Astron. Soc. Pac.* **117**, 1144–1171 (2005).
15. J. den Herder et al., "The reflection grating spectrometer on board XMM-Newton," *Astron. Astrophys.* **365**, L7–L17 (2001).
16. H. M. Günther et al., "Ray-tracing Arcus in phase A," *Proc. SPIE* **10699**, 106996F (2018).
17. A. Bruccoleri et al., "Potassium hydroxide polishing of nanoscale deep reactive-ion etched ultrahigh aspect ratio gratings," *J. Vac. Sci. Technol. B* **31**, 06FF02 (2013).
18. R. K. Heilmann et al., "Blazed high-efficiency x-ray diffraction via transmission through arrays of nanometer-scale mirrors," *Opt. Express* **16**, 8658–8669 (2008).
19. R. K. Heilmann et al., "Manufacture and performance of blazed soft x-ray transmission gratings for Arcus and Lynx," *Proc. SPIE* **11822**, 1182215 (2021).
20. A. R. Bruccoleri, R. K. Heilmann, and M. L. Schattenburg, "Fabrication process for 200 nm-pitch polished freestanding ultrahigh aspect ratio gratings," *J. Vac. Sci. Technol. B* **34**, 06KD02 (2016).
21. R. K. Heilmann et al., "Toward volume manufacturing of high-performance soft x-ray critical-angle transmission gratings," *Proc. SPIE* **11444**, 114441H (2021).
22. M. Moharam et al., "Stable implementation of the rigorous coupled-wave analysis for surface-relief gratings - enhanced transmittance matrix approach," *J. Opt. Soc. Amer. A-Opt. Image Sci. Vis.* **12**, 1077–1086 (1995).
23. R. K. Heilmann et al., "Critical-angle transmission grating technology development for high resolving power soft x-ray spectrometers on Arcus and Lynx," *Proc. SPIE* **10399**, 1039914 (2017).
24. H. M. Günther, "Ray-tracing Arcus for performance and alignment tolerances," *Proc. SPIE* **12678**, 126781D (2023).
25. R. K. Heilmann et al., "Critical-angle x-ray transmission grating spectrometer with extended bandpass and resolving power $>$ 10,000," *Proc. SPIE* **9905**, 99051X (2016).
26. R. K. Heilmann et al., "X-ray performance of critical-angle transmission grating prototypes for the Arcus mission," *Astrophys. J.* **934**, 171 (2022).
27. R. K. Heilmann et al., "Demonstration of resolving power $\lambda/\Delta\lambda > 10,000$ for a space-based x-ray transmission grating spectrometer," *Appl. Opt.* **58**, 1223–1238 (2019).
28. P. Predehl et al., "Grating elements for the AXAF low-energy transmission grating spectrometer," *Proc. SPIE* **1743**, 475–481 (1992).
29. H. L. Marshall, "Updating the Chandra HETGS efficiencies using in-orbit observations," *Proc. SPIE* **8443**, 844348 (2012).
30. R. K. Heilmann et al., "Soft x-ray performance and fabrication of flight-like blazed transmission gratings for the x-ray spectrometer on Arcus Probe," *Proc. SPIE* **12679**, 126790L (2023).
31. Y. Ishisaki et al., "Status of resolve instrument onboard X-ray imaging and spectroscopy mission (XRISM)," *Proc. SPIE* **12181**, 121811S (2022).
32. J. Song et al., "Characterizing profile tilt of nanoscale deep-etched gratings via x-ray diffraction," *J. Vac. Sci. Technol. B* **37**, 062917 (2019).
33. R. K. Heilmann et al., "Flight-like critical-angle transmission grating x-ray performance for Arcus," *Proc. SPIE* **12181**, 1218116 (2022).
34. R. K. Heilmann et al., "Progress in x-ray critical-angle transmission grating technology development," *Proc. SPIE* **11119**, 1111913 (2019).
35. J. A. Gaskin et al., "Lynx x-ray observatory: an overview," *J. Astron. Telesc. Instrum. Syst.* **5**(2), 021001 (2019).
36. H. M. Günther and R. K. Heilmann, "Lynx soft x-ray critical-angle transmission grating spectrometer," *J. Astron. Telesc. Instrum. Syst.* **5**(2), 021003 (2019).
37. P. Cheimets et al., "Co-alignment methodology for the x-ray and UV spectrometers on Arcus probe," *J. Astron. Telesc. Instrum. Syst.* **11**(1) (2025).

38. K. France et al., "Arcus ultraviolet spectrograph: enabling far-ultraviolet spectroscopy with the Arcus X-ray probe," *J. Astron. Telesc. Instrum. Syst.* **11**(1) (2025).

Ralf K. Heilmann is a principal research scientist at the MIT Kavli Institute for Astrophysics and Space Research and the associate director of the Space Nanotechnology Laboratory (SNL). He received his diploma in physics from the FAU Erlangen/Nürnberg (1991) and his MS (1993) and PhD (1996) in physics from Carnegie Mellon University. After a postdoc at Harvard, he joined the SNL and has since focused on advanced lithography and the development of X-ray optics for astronomy. He is a senior member of SPIE.

Hans Moritz Günther is a research scientist at MIT. He received his undergraduate degree (in 2005) and his PhD (in 2009) in physics from the University of Hamburg, Germany. After that, he worked at the Harvard-Smithsonian Center for Astrophysics and came to MIT in 2015. He is currently the lead developer of MARX, the ray-tracing software used for the Chandra X-ray observatory. His science interests are in star formation using data from the radio to X-rays.

Mark L. Schattenburg is a senior research scientist at the MIT Kavli Institute for Astrophysics and Space Research and director of the Space Nanotechnology Laboratory (SNL). He received his PhD in physics from MIT (1984). He is a fellow of Optica.

Biographies of the other authors are not available.